Progress In Electromagnetics Research, Vol. 107, 1–20, 2010

GREEN'S TENSORS FOR THE DIFFUSIVE ELECTRIC FIELD IN A VTI HALF-SPACE

E. Slob, J. Hunziker, and W. A. Mulder †

Department of Geotechnology
Delft University of Technology (TU Delft)
Stevinweg 1, 2628 CN Delft, The Netherlands

Abstract—Explicit Green's tensors for the diffusive electric field in a configuration with two homogeneous half spaces are of interest for primary-secondary formulations of frequency domain and time domain modeling schemes. We derive the explicit expressions for the Green tensor of the electric field generated by an electric dipole in space frequency and space time. Both source and receiver can have arbitrary positions in the vertical transverse isotropic (VTI) half space below a non conductive half space. Apart from their use in modeling schemes, the expressions can be used to understand the effect of the interface between the VTI and the non conducting half space. We show that the TE-mode refracts against the interface, and its effect in the VTI half space decays exponentially as a function of depth and is inversely proportional to horizontal distance cubed for horizontal source receiver distances larger than three times the source depth. In exploration geophysics, this part of the field is known as the "airwave". The contribution from the "airwave" has a late time behavior that differs from the other contributions to the electric field. This makes time domain systems relevant for exploration geophysical applications.

1. INTRODUCTION

Transient and frequency domain electromagnetic methods have potential for hydrocarbon exploration in marine environments and on land [1–3]. Solutions for the two half spaces configuration are of interest in electric field integral equation solutions and approximations thereof [4–8]. Such solutions are also important for modeling by

Received 28 May 2010, Accepted 19 July 2010, Scheduled 28 July 2010
Corresponding author: E. Slob (e.c.slob@tudelft.nl).
† W. A. Mulder is also with Shell International Exploration and Production B.V., P. O. Box 60, 2280 AB Rijswijk, The Netherlands.

local methods such as finite-difference, finite-element and finite-volume methods [9–12] as well as for inversion methods based on local forward-modeling schemes [13–16]. Using a primary-secondary solution procedure with local numerical methods reduces the necessity for small grid spacings for the direct field, allows for more accurate incorporation of the source, and computes the desired target response at greater accuracy. Explicit expressions for the isotropic half space response tensor in the frequency domain have been known for 35 years [17]. Here, we make an extension to a conducting VTI lower half space and we give explicit solutions in the frequency domain as well as in the time domain.

The configuration consists of two half spaces separated at $z = 0$ by an interface. The upper half space is an isotropic medium, with conductivity σ_0, and is present for $z < 0$. We use the diffusive approximation also in the non conductive upper half space and take $\sigma_0 = 0\,\mathrm{S/m}$. The lower half space, $z > 0$, is a non-magnetic VTI medium, characterized by horizontal conductivity σ and vertical conductivity σ_v. The electric dipole source is present at depth z^S below the origin, at $\mathbf{x}^S = (0, 0, z^S)$, $z^S > 0$. The receiver can be anywhere in the VTI half space, at $(x, y) \in \mathbb{R}^2$, $z \geq 0$. The magnetic permeability is constant throughout the configuration and given by its free space value, μ_0. We use $\zeta = s\mu_0$, where s denotes the Laplace transformation parameter. The product of σ and ζ is the squared vertical wave number of the lower half space, $\gamma = \sqrt{\zeta\sigma}$ and $\gamma_v = \sqrt{\zeta\sigma_v}$. We also introduce the geometrical mean conductivity, $\bar{\sigma} = \sqrt{\sigma\sigma_v}$ and the anisotropy coefficient $\lambda = \sqrt{\sigma/\sigma_v}$.

Throughout the manuscript, subscript notation is used for Cartesian tensors wherever convenient, the summation convention is applied to repeated subscripts, and the lower case Greek subscripts run over the values $(1, 2)$, while lower case Latin subscripts run over the values $(1, 2, 3)$. In the domain of the horizontal wave number, the electric field Green tensor for an electric dipole in the VTI half space is known. It is obtained from solving the following set of equations for the electric field

$$\epsilon_{\alpha\beta3} ik_\beta \tilde{H}_3 - \epsilon_{\alpha3\nu}\partial_3 \tilde{H}_\nu + \sigma\tilde{E}_\alpha = -\tilde{J}^e_\alpha, \tag{1}$$

$$\epsilon_{3\alpha\beta} ik_\alpha \tilde{H}_\beta + \sigma_v \tilde{E}_3 = -\tilde{J}^e_3, \tag{2}$$

$$\epsilon_{\alpha\beta3} ik_\beta \tilde{E}_3 - \epsilon_{\alpha3\nu}\partial_3 \tilde{E}_\nu - \zeta\tilde{H}_\alpha = 0, \tag{3}$$

$$\epsilon_{3\alpha\beta} ik_\alpha \tilde{E}_\beta - \zeta\tilde{H}_3 = 0, \tag{4}$$

where $\epsilon_{ikr} = 1$ for $ikr = 123, 231, 312$, $\epsilon_{ikr} = -1$ for $ikr = 132, 321, 213$, and it is zero otherwise, and k_α denotes the two components of the horizontal wave number vector. The

boundary conditions require the horizontal electric and magnetic field components to be continuous across the interface $z = 0$. The solution for the electric field Green function is then found by taking the source to be a Dirac function, $\tilde{J}_k^e(z) = \delta_{kr}\delta(z - z^S)$, which extends the vector electric field to a Green tensor. The space frequency domain results can be written as Fourier-Bessel transformations of these horizontal wave number domain expressions. The horizontal distance in space is denoted $\rho = \sqrt{x^2 + y^2}$. The scaled vertical distances from source to receiver are denoted $\bar{h}^{\pm} = |z \pm z^S|\lambda$, whereas the physical vertical distances from source to receiver are denoted $h^{\pm} = |z \pm z^S|$. In these expressions, the superscripted minus sign indicates the direct distance, whereas the superscripted plus sign denotes the vertical distance from source to receiver via the surface. We need radial distances from source to receiver given by $\bar{r}^{\pm} = \sqrt{\rho^2 + (\bar{h}^{\pm})^2}$ and $r = \sqrt{\rho^2 + (h^{\pm})^2}$.

2. THE HORIZONTAL WAVE NUMBER FREQUENCY DOMAIN ELECTRIC FIELD

Using the formalism of [18], the electric field Green tensor can be written in components as

$$\begin{aligned}\tilde{G}_{\alpha\beta} &= ik_\alpha ik_\beta \left(\frac{1}{\sigma_v} + \frac{\zeta}{\kappa^2}\right)\left(\tilde{\bar{G}}^- + r^{\mathrm{TM}}\tilde{\bar{G}}^+\right) \\ &\quad -\zeta\frac{ik_\alpha ik_\beta + \kappa^2\delta_{\alpha\beta}}{\kappa^2}\left(\tilde{G}^- - r^{\mathrm{TE}}\tilde{G}^+\right), \end{aligned} \tag{5}$$

where $\kappa = \sqrt{k_1^2 + k_2^2}$ is the radial wave number. The vertical components are given by

$$\tilde{G}_{3\beta} = -\frac{ik_\beta\partial_3}{\sigma_v}\left(\tilde{\bar{G}}^- + r^{\mathrm{TM}}\tilde{\bar{G}}^+\right), \tag{6}$$

$$\tilde{G}_{33} = \frac{\partial_3\partial_3 - \gamma^2}{\sigma_v}\left(\tilde{\bar{G}}^- - r^{\mathrm{TM}}\tilde{\bar{G}}^+\right). \tag{7}$$

The TM-mode and TE-mode scalar Green functions are given by

$$\tilde{\bar{G}}^{\pm} = \frac{\exp\left(-\bar{\Gamma}h^{\pm}\right)}{2\bar{\Gamma}}, \quad \tilde{G}^{\pm} = \frac{\exp\left(-\Gamma h^{\pm}\right)}{2\Gamma}, \tag{8}$$

respectively. The vertical plane wave numbers are given by $\bar{\Gamma} = \sqrt{\sigma\kappa^2/\sigma_v + \gamma^2}$ and $\Gamma = \sqrt{\kappa^2 + \gamma^2}$. In the diffusive approximation the TM-mode and TE-mode reflection coefficients are given by

$$r^{\mathrm{TM}} = 1, \quad r^{\mathrm{TE}} = \frac{\kappa - \Gamma}{\kappa + \Gamma} = -1 - 2\frac{\kappa^2}{\sigma\zeta} + 2\frac{\kappa\Gamma}{\sigma\zeta}. \tag{9}$$

Substituting these results in Equations (5)–(7) yields

$$\tilde{G}_{\alpha\beta} = ik_\alpha ik_\beta \left(\frac{1}{\sigma_v} + \frac{\zeta}{\kappa^2}\right)\left(\tilde{\bar{G}}^- + \tilde{\bar{G}}^+\right) - \left(ik_\alpha ik_\beta + \kappa^2\delta_{\alpha\beta}\right)\left[\frac{\zeta}{\kappa^2}\left(\tilde{G}^- + \tilde{G}^+\right) + \frac{2}{\sigma}\left(1 + \frac{\partial_3}{\kappa}\right)\tilde{G}^+\right]. \quad (10)$$

The vertical components are given by

$$\tilde{G}_{3\beta} = -\frac{ik_\beta\partial_3}{\sigma_v}\left(\tilde{\bar{G}}^- + \tilde{\bar{G}}^+\right), \quad \tilde{G}_{33} = \frac{\partial_3\partial_3 - \gamma^2}{\sigma_v}\left(\tilde{\bar{G}}^- - \tilde{\bar{G}}^+\right). \quad (11)$$

These functions can be transformed back to the space frequency domain in explicit form. The general procedure is to write the two-dimensional inverse spatial Fourier transformations in cylindrical coordinates. The transform of a wave number domain scalar Green function $\tilde{G}$ is given by

$$\hat{G}\left(\boldsymbol{x}, \boldsymbol{x}', \omega\right) = \frac{1}{2\pi}\int_{\kappa=0}^{\infty} \tilde{G}\left(\kappa, z, z^S\right) J_0(\kappa\rho)\, \kappa d\kappa, \quad (12)$$

and with the known Sommerfeld integral

$$\frac{\exp\left(-\gamma r^\pm\right)}{4\pi r^\pm} = \frac{1}{2\pi}\int_{\kappa=0}^{\infty} \frac{\exp\left(-\Gamma h^\pm\right)}{2\Gamma} J_0(\kappa\rho)\kappa d\kappa, \quad (13)$$

and the fact that $-ik_\alpha$ transforms to ∂_α, all parts containing scalar Green's functions can be directly transformed to space frequency domain. The terms where the Green's function are divided by κ or by κ^2 must be done separately and are discussed in the next section.

3. THE SPACE FREQUENCY DOMAIN ELECTRIC FIELD

As shown above, we can write the electric field generated by an electric dipole in terms of Fourier-Bessel transforms. In view of Equations (10) and (11) and the result of Equation (13), two Green's functions can be defined

$$\hat{\bar{G}}^\pm = \frac{\exp\left(-\gamma_v \bar{r}^\pm\right)}{4\pi\lambda\bar{r}^\pm}, \quad \hat{G}^\pm = \frac{\exp\left(-\gamma r^\pm\right)}{4\pi r^\pm}. \quad (14)$$

The expressions containing the factor κ^{-n}, with $n = 1, 2$ need to be elaborated on. We observe that $ik_\beta\tilde{G}^+/\kappa^2$ leads to the following inverse spatial Fourier transformation

$$-\frac{\partial_\beta}{4\pi}\int_{\kappa=0}^{\infty}\frac{\exp(-\Gamma h^+)}{\Gamma\kappa}J_0(\kappa\rho)d\kappa = \frac{x_\beta}{4\pi\rho}\int_{\kappa=0}^{\infty}\frac{\exp(-\Gamma h^+)}{\Gamma}J_1(\kappa\rho)d\kappa = \frac{x_\beta}{4\pi\rho}I_{1/2}(\xi^-)K_{1/2}(\xi^+), \quad (15)$$

with $\xi^{\pm} = \gamma(r^+ \pm h^+)/2$. This result is found from [19] (p. 1098, formula 6.637.1). This form contains spherical Bessel functions and can be written as

$$I_{1/2}\left(\xi^-\right) K_{1/2}(\xi^+) = \frac{\exp\left(-\gamma h^+\right) - \exp\left(-\gamma r^+\right)}{\gamma\rho}, \tag{16}$$

see [20]. Similar results are obtained for the other Green functions containing the factor κ^{-2}. The expression $\tilde{G}^+/\kappa$ can directly be obtained as

$$\frac{1}{4\pi}\int_{\kappa=0}^{\infty} \frac{\exp\left(-\Gamma h^+\right)}{\Gamma} J_0(\kappa\rho)d\kappa = \frac{x_\beta}{4\pi\rho} I_0\left(\xi^-\right) K_0\left(\xi^+\right). \tag{17}$$

With these integrals the whole electromagnetic field can be determined in the VTI half space. All terms of Equations (10) and (11) can be transformed back to the space domain using the formulas given above. The horizontal components of the electric field generated by horizontal components of an electric dipole source can be written as

$$\begin{aligned}\hat{G}_{\alpha\beta}\left(\boldsymbol{x},\boldsymbol{x}',s\right) = {} & \frac{\partial_\alpha\partial_\beta}{\sigma_v}\left(\hat{\tilde{G}}^-\left(\boldsymbol{x},\boldsymbol{x}',s\right) + \hat{\tilde{G}}^+\left(\boldsymbol{x},\boldsymbol{x}',s\right)\right) \\ & + \frac{\zeta\partial_\alpha}{4\pi\gamma}\frac{x_\beta}{\rho^2}\left[\exp\left(-\gamma_v\bar{r}^-\right) + \exp\left(-\gamma_v\bar{r}^+\right) - \exp\left(-\gamma r^-\right)\right. \\ & \left. - \exp\left(-\gamma r^+\right)\right] + \zeta\delta_{\alpha\beta}\left(\hat{G}^-\left(\boldsymbol{x},\boldsymbol{x}',s\right) + \hat{G}^+\left(\boldsymbol{x},\boldsymbol{x}',s\right)\right) \\ & - \frac{2}{\sigma}(\partial_\alpha\partial_\beta - \partial_\nu\partial_\nu\delta_{\alpha\beta})\left(\hat{G}^+\left(\boldsymbol{x},\boldsymbol{x}',s\right) + I_0\left(\xi^-\right)K_0\left(\xi^+\right)\right). \end{aligned} \tag{18}$$

The vertical field components are written as

$$\hat{G}_{3\beta}\left(\boldsymbol{x},\boldsymbol{x}',s\right) = \frac{\partial_3\partial_\beta}{\sigma_v}\left(\hat{\tilde{G}}^-\left(\boldsymbol{x},\boldsymbol{x}',s\right) + \hat{\tilde{G}}^+\left(\boldsymbol{x},\boldsymbol{x}',s\right)\right), \tag{19}$$

$$\hat{G}_{33}\left(\boldsymbol{x},\boldsymbol{x}',s\right) = \frac{-\gamma^2 + \partial_3\partial_3}{\sigma_v}\left(\hat{\tilde{G}}^-\left(\boldsymbol{x},\boldsymbol{x}',s\right) - \hat{\tilde{G}}^+\left(\boldsymbol{x},\boldsymbol{x}',s\right)\right). \tag{20}$$

These expressions can be understood geometrically as follows. All terms depending on products of polynomial and exponential functions are direct fields from source to receiver, or specular reflections against the surface. The direct fields have function arguments depending on r^- or $\bar{r}^-$. The specular reflections have function arguments depending on r^+ or $\bar{r}^+$, which can be understood as fields from an image source above the actual source location, for which reason they can be seen as specular reflections against the surface. The parts of the Green tensor that have one or two vertical components are completely described by these functions. The parts of the Green tensor that have two horizontal components have an additional term in the form of the product of two

Bessel functions. For large arguments, and where ($r^+ \gg h^+$), this product has an exponential decay as a function of h^+ and a polynomial decay as a function of two terms involving the horizontal distance, ρ^{-2n} and $(h^+/\rho^2)^n$, where n is the counter for the expansion terms. This behavior can be understood physically as the diffusive field that decays vertically upward, propagates as a wave with infinite speed along the surface, with only geometrical spreading, and continuously diffuses down into the subsurface with exponential decay in the vertical direction. This is found when an asymptotic expansion is carried out for large arguments of both Bessel functions. The leading term is given by

$$\lim_{\gamma r^+ \to \infty} I_0\left(\xi^-\right) K_0\left(\xi^+\right) \approx \frac{\exp\left(-\gamma h^+\right)}{\gamma\rho}\left(1 + \mathcal{O}\left(\rho^{-2}\right)\right). \tag{21}$$

From the observation that two horizontal derivatives occur in Equation (18), we can expect that for a single frequency of operation, the airwave effect in the subsurface has a large horizontal offset asymptote proportional to ρ^{-3}.

The Green tensor can be written concisely in terms of frequency independent coefficients and frequency dependent diffusion functions, given in Equation (A1). Then we obtain

$$\begin{aligned}\hat{G}^{ee}_{kr}\left(\boldsymbol{x}, \boldsymbol{x}', s\right) = \hat{P}_{kr}(s,\xi) + \sum_{m=0}^{2}\Big(&g^{m-}_{kr}\hat{F}^{(m)}(s,\tau^-) + g^{m+}_{kr}\hat{F}^{(m)}(s,\tau^+) \\ &+ \bar{g}^{m-}_{kr}\hat{F}^{(m)}(s,\bar{\tau}^-) + \bar{g}^{m+}_{kr}\hat{F}^{(m)}(s,\bar{\tau}^+)\Big).\end{aligned} \tag{22}$$

The offset dependent diffusion times $\tau^\pm$ and $\tau^\pm_v$ are given by

$$\tau^\pm = \sigma\mu_0(r^\pm)^2/4, \quad \bar{\tau}^\pm = \sigma\mu_0(\bar{r}^\pm)^2/4. \tag{23}$$

The TM-mode coefficients for the horizontal components are given by

$$\bar{g}^{0\pm}_{\alpha\beta}\left(\boldsymbol{x}, \boldsymbol{x}^S\right) = \lambda\frac{3x_\alpha x_\beta - (\bar{r}^\pm)^2\delta_{\alpha\beta}}{4\pi\sigma(\bar{r}^\pm)^5}, \tag{24}$$

$$\bar{g}^{1\pm}_{\alpha\beta}\left(\boldsymbol{x}, \boldsymbol{x}^S\right) = \left(\frac{3x_\alpha x_\beta - (\bar{r}^\pm)^2\delta_{\alpha\beta}}{4\pi(\bar{r}^\pm)^4} - \frac{2x_\alpha x_\beta - \rho^2\delta_{\alpha\beta}}{4\pi\rho^4}\right)\frac{\sqrt{\mu_0}}{\sqrt{\sigma}}, \tag{25}$$

$$\bar{g}^{2\pm}_{\alpha\beta}\left(\boldsymbol{x}, \boldsymbol{x}^S\right) = \frac{\mu_0 x_\alpha x_\beta}{4\pi\lambda\bar{r}^\pm}\left(\frac{1}{(\bar{r}^\pm)^2} - \frac{1}{\rho^2}\right). \tag{26}$$

The numerical singularity at zero horizontal offset is avoided by taking the limit of $\rho \to 0$ for $z \neq z^S$, which results in

$$\bar{g}^{1\pm}_{\alpha\beta}\left(z, z^S\right) = -\frac{\sqrt{\mu_0}\delta_{\alpha\beta}}{4\pi\sqrt{\sigma}(\lambda h^\pm)^2}, \quad \bar{g}^{2\pm}_{\alpha\beta}\left(z, z^S\right) = -\frac{\delta_{\alpha\beta}\mu_0}{8\pi\lambda^2 h^\pm}. \tag{27}$$

The TE-mode coefficients are given by

$$g_{\alpha\beta}^{0-}\left(\boldsymbol{x},\boldsymbol{x}^S\right)=0,\quad g_{\alpha\beta}^{0+}\left(\boldsymbol{x},\boldsymbol{x}^S\right)=\frac{3f_{\alpha\beta}-(r^+)^2\delta_{\alpha\beta}}{2\pi\sigma(r^+)^5}, \tag{28}$$

$$g_{\alpha\beta}^{1-}\left(\boldsymbol{x},\boldsymbol{x}^S\right)=\frac{x_\alpha x_\beta-f_{\alpha\beta}}{4\pi\rho^4}\frac{\sqrt{\mu_0}}{\sqrt{\sigma}}, \tag{29}$$

$$g_{\alpha\beta}^{1+}\left(\boldsymbol{x},\boldsymbol{x}^S\right)=\left(\frac{3f_{\alpha\beta}-(r^+)^2\delta_{\alpha\beta}}{2\pi\sqrt{\sigma}(r^+)^4}+\frac{x_\alpha x_\beta-f_{\alpha\beta}}{4\pi\rho^4}\right)\frac{\sqrt{\mu_0}}{\sqrt{\sigma}}, \tag{30}$$

$$g_{\alpha\beta}^{2-}\left(\boldsymbol{x},\boldsymbol{x}^S\right)=-\frac{\mu_0 f_{\alpha\beta}}{4\pi\rho^2 r^-}, \tag{31}$$

$$g_{\alpha\beta}^{2+}\left(\boldsymbol{x},\boldsymbol{x}^S\right)=\frac{\mu_0 f_{\alpha\beta}}{4\pi r^+}\left(\frac{2}{(r^+)^2}-\frac{1}{\rho^2}\right), \tag{32}$$

with $f_{\alpha\beta}=(\rho^2\delta_{\alpha\beta}-x_\alpha x_\beta)$. In the limit of $\rho\to 0$ for $h^-\neq 0$ the TE-mode coefficients containing divisions by ρ reduce to

$$g_{\alpha\beta}^{1-}\left(z,z^S\right)=0,\qquad g_{\alpha\beta}^{2-}\left(z,z^S\right)=\frac{\delta_{\alpha\beta}\mu_0}{8\pi h^+}, \tag{33}$$

$$g_{\alpha\beta}^{1+}\left(z,z^S\right)=-\frac{\sqrt{\mu_0}\delta_{\alpha\beta}}{2\pi\sqrt{\sigma}(h^+)^2},\quad g_{\alpha\beta}^{2+}\left(z,z^S\right)=\frac{\delta_{\alpha\beta}\mu_0}{8\pi h^+}. \tag{34}$$

Note that in that case $\bar{\tau}^\pm=\tau^\pm$. The function $\hat{P}$ describes the effect of the airwave in the subsurface, and contains modified Bessel functions of integer order. It is given by

$$\begin{aligned}&\hat{P}_{\alpha\beta}\big(\boldsymbol{x},\boldsymbol{x}^S,s\big)\\&=\frac{\gamma\zeta f_{\alpha\beta}h^+}{16\pi(r^+)^3}\left[4I_1K_0-\left(3I_0-2I_1/\xi^+ +I_2\right)K_1\right]\\&\quad-\left(\frac{3f_{\alpha\beta}}{(r^+)^2}-\delta_{\alpha\beta}\right)\frac{\gamma^2h^+r^+(I_0K_0-I_1K_1)+2\xi^+I_0K_1+2\xi^-I_1K_0}{4\pi\sigma(r^+)^3},\end{aligned} \tag{35}$$

and all other coefficients are zero. The arguments of the Bessel functions have been omitted for brevity.

In the numerical implementation, scaled Bessel functions provide more accurate results. We use

$$\bar{I}_n(\xi^-)=\exp\left(-\Re\{\xi^-\}\right)I_n(\xi^-), \tag{36}$$

$$\bar{K}_n(\xi^-)=\exp(\xi^+)K_n(\xi^-), \tag{37}$$

where $\Re\{\xi\}$ means the real part of ξ. For any product containing modified Bessel functions of the first and second kind, we have

$$I_n(\xi^-)K_m(\xi^+)=\exp\left(-\Re\{\gamma\}h^+-i\Im\{\xi^+\}\right)\bar{I}_n(\xi^-)\bar{K}_m(\xi^+). \tag{38}$$

The coefficients of the vertical Green functions are given by

$$\bar{g}^{0-}_{3\alpha}\left(\boldsymbol{x},\boldsymbol{x}^S\right)=\frac{3x_\alpha(z-z^S)}{4\pi\sigma_v(\bar{r}^-)^5},\qquad \bar{g}^{0+}_{3\alpha}\left(\boldsymbol{x},\boldsymbol{x}^S\right)=\frac{3x_\alpha h^+}{4\pi\sigma_v(\bar{r}^+)^5}, \tag{39}$$

$$\bar{g}^{1-}_{3\alpha}\left(\boldsymbol{x},\boldsymbol{x}^S\right)=\sqrt{\frac{\mu_0}{\sigma_v}}\frac{3x_\alpha(z-z^S)}{4\pi(\bar{r}^-)^4},\ \bar{g}^{1+}_{3\alpha}\left(\boldsymbol{x},\boldsymbol{x}^S\right)=\sqrt{\frac{\mu_0}{\sigma_v}}\frac{3x_\alpha h^+}{4\pi(\bar{r}^+)^4}, \tag{40}$$

$$\bar{g}^{2-}_{3\alpha}\left(\boldsymbol{x},\boldsymbol{x}^S\right)=\mu_0\frac{x_\alpha(z-z^S)}{4\pi(\bar{r}^-)^3},\qquad \bar{g}^{2+}_{3\alpha}\left(\boldsymbol{x},\boldsymbol{x}^S\right)=\mu_0\frac{x_\alpha h^+}{4\pi(\bar{r}^+)^3}, \tag{41}$$

and in view of reciprocity,

$$\bar{g}^{m-}_{\alpha 3}\left(\boldsymbol{x},\boldsymbol{x}^S\right)=\bar{g}^{m-}_{3\alpha}\left(\boldsymbol{x},\boldsymbol{x}^S\right),\quad \bar{g}^{m+}_{\alpha 3}\left(\boldsymbol{x},\boldsymbol{x}^S\right)=-\bar{g}^{m+}_{3\alpha}\left(\boldsymbol{x},\boldsymbol{x}^S\right), \tag{42}$$

for $m=0$, 1, 2. The last coefficients are found as

$$\bar{g}^{0\pm}_{33}\left(\boldsymbol{x},\boldsymbol{x}^S\right)=\mp\frac{\left[3\lambda(\bar{h}^\pm)^2-(\bar{r}^\pm)^2\right]}{4\pi\sigma_v(\bar{r}^\pm)^5}, \tag{43}$$

$$\bar{g}^{1\pm}_{33}\left(\boldsymbol{x},\boldsymbol{x}^S\right)=\mp\sqrt{\frac{\mu_0}{\sigma_v}}\frac{\left[3\lambda(h^\pm)^2-(\bar{r}^\pm)^2\right]}{4\pi(\bar{r}^\pm)^4}, \tag{44}$$

$$\bar{g}^{2\pm}_{33}\left(\boldsymbol{x},\boldsymbol{x}^S\right)=\mp\mu_0\lambda\frac{\left[(h^\pm_v)^2-(\bar{r}^\pm)^2\right]}{4\pi(\bar{r}^\pm)^3}. \tag{45}$$

These coefficients determine the electric field, as there is no TE-mode in the vertical components and all coefficients $g^{m\pm}_{3k}$ are zero for $k=\{1,\,2,\,3\}$ and $m=\{0,\,1,\,2\}$.

4. THE TIME DOMAIN ELECTRIC FIELD

The impulse response function of the electric fields are, with the aid of the diffusion functions defined in Equations (A3)–(A7), written as

$$\begin{aligned}G^{ee}_{kr}\left(\boldsymbol{x},\boldsymbol{x}^S,t\right) \;=\; & P_{kr}(t,\tau)+\sum_{m=0}^{2}\Big(g^-_{kr;m}F^{(m)}(t,\tau^-)+g^+_{kr;m}F^{(m)}(t,\tau^+)\\ & +\bar{g}^-_{kr;m}F^{(m)}(t,\bar{\tau}^-)+\bar{g}^+_{kr;m}F^{(m)}(t,\bar{\tau}^+)\Big).\end{aligned} \tag{46}$$

The horizontal components of the TM-mode coefficients are given in Equations (24)–(26), and those for the TE-mode in Equations (28)–(32). The vertical components are described by the TM-mode coefficients of Equations (39)–(45). The Laplace transform pair exists for the product of the two Bessel functions of equal order [21], (p. 346),

$$I_0(\xi^-)K_0(\xi^+)\overset{\mathcal{L}^{-1}}{\longleftrightarrow}\frac{\exp\left(-\tau_h^+/t-\tau_\rho/t\right)I_0(\tau_\rho/t)}{2t}=\frac{\exp\left(-\tau_h^+/t\right)\bar{I}_0\left(\tau_\rho/t\right)}{2t},$$

with

$$\tau_h^+ = \sigma\mu_0(h^+)^2/4, \tag{47}$$

$$\tau_\rho = \sigma\mu_0\rho^2/8. \tag{48}$$

This leads to the space time expression for the subsurface effect of the airwave given by

$$P_{\alpha\beta}(t,\tau) = \frac{(\partial_\nu\partial_\nu\delta_{\alpha\beta} - \partial_\alpha\partial_\beta)\partial_z}{4\pi\sigma t}\bar{I}_0(\tau_\rho/t)\exp(-\tau_h^+/t). \tag{49}$$

$$P_{\alpha\beta}(t,\tau) = \frac{\sigma\mu_0^2 h^+\exp(-\tau_h^+/t)}{32\pi t^3}\left\{2\left(\delta_{\alpha\beta} - \frac{x_\alpha x_\beta}{\rho^2}\right)\bar{I}_1(\tau_\rho/t) - \left(\frac{\sigma\mu_0}{2t}\left(\rho^2\delta_{\alpha\beta} - x_\alpha x_\beta\right) - \delta_{\alpha\beta}\right)\left(\bar{I}_0(\tau_\rho/t) - \bar{I}_1(\tau_\rho/t)\right)\right\}. \tag{50}$$

All other coefficients and function components are zero. The late time asymptotes of the Bessel functions occurring in Equation (50) are given by

$$\lim_{\tau_\rho/t\to 0}\bar{I}_n(\tau_\rho/t) = \frac{\tau_\rho^n}{n!(2t)^n}. \tag{51}$$

From this result and Equation (50) it can be seen that P_{11} and P_{22} have a late time asymptote proportional to t^{-3}, whereas P_{12} and P_{21} have a late time asymptote proportional to t^{-4} when both $x_1 \neq 0$ and $x_2 \neq 0$, otherwise $P_{12} = P_{21} = 0$.

Sometimes, the impulse response is obtained in transient electromagnetic methods, but often the source current is switched on and off and step responses are obtained. For the diffusion functions this poses no problem, because every function $F^m(t,\tau)$ can be replaced by $F^{(m-2)}(t,\tau)$ and they are all known. For the airwave effect no explicit formula could be found. A quasi analytic result is obtained using the Gaver-Stehfest [22, 23] method that computes a time function from the Laplace domain function using a number of time values instead of the Laplace parameter s. For a step current switch-on source, the airwave effect can be computed in the time domain as

$$P_{\alpha\beta}^H(t,\tau) = t\sum_{k=1}^{K} D_k\hat{P}_{\alpha\beta}(s = k\log(2)/t,\tau)/(k\log(2)), \tag{52}$$

where $\hat{P}_{\alpha\beta}(s,\tau)$ is given in Equation (35). The value of K is determined by the accuracy of the Laplace domain numerical result. For double precision arithmetic, $K = 14$ or $K = 16$ can be used. The coefficients D_k are given by

$$D_k = \sum_{n=(k+1)/2}^{\min(k,K/2)} \frac{n^{K/2}(2n)!}{n!(n-1)!(k-n)!(2n-k)!(K/2-n)!}. \tag{53}$$

The response to a step current switch-off source can then be obtained by subtracting the result of the step current switch-on source from the result of the step current switch-on source computed for a very large time value.

5. NUMERICAL RESULTS

Here we use (x, y, z) to denote coordinates in space, with $x = x_1$, $y = x_2$ and $z = x_3$. As an example a homogeneous half space is taken with $\sigma = 1\,\mathrm{S/m}$ and $\sigma_v = 0.2\,\mathrm{S/m}$. Most applications use a single frequency of the source signal and here $f = 0.5\,\mathrm{Hz}$ is used. The non-conductive upper half space is bounded by the VTI half space at $z = 0$ and the z-axis is taken positive downward. The horizontal electric dipole source is 200 m long, located at $(-100 < x < 100,\ y = 0,\ z = 200)\,\mathrm{m}$, or at $(-100 < x < 100,\ 0,\ 1000)\,\mathrm{m}$, and the receivers are located in the (x, z)-plane, $(0 < x < 10,\ 0,\ 0 < z < 4)\,\mathrm{km}$. The results are shown in Figure 1 for a source depth of 200 m in (a) and (b) and for a source depth of 1 km in (c) and (d). The left and right columns of Figure 1, respectively, depict the real and imaginary parts of the electric field vector. It can be seen that the shallow source produces a relatively strong field close to the surface, which is recognized as the effect of the airwave just above the surface in the non-conductive medium. To see the strengths of the different

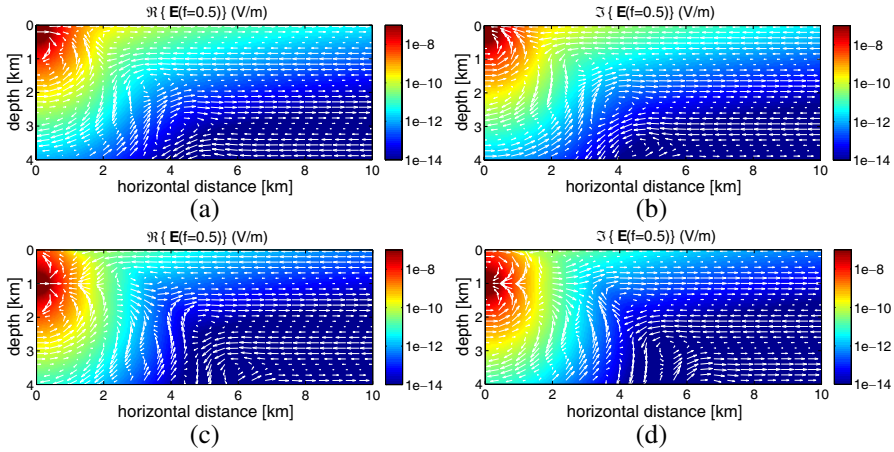

Figure 1. The real (a), (c) and imaginary (b), (d) parts of the electric field vector in the (x, z)-plane for an x-directed electric dipole located at a depth of 200 m (a), (b) and at a depth of 1 km (c), (d).

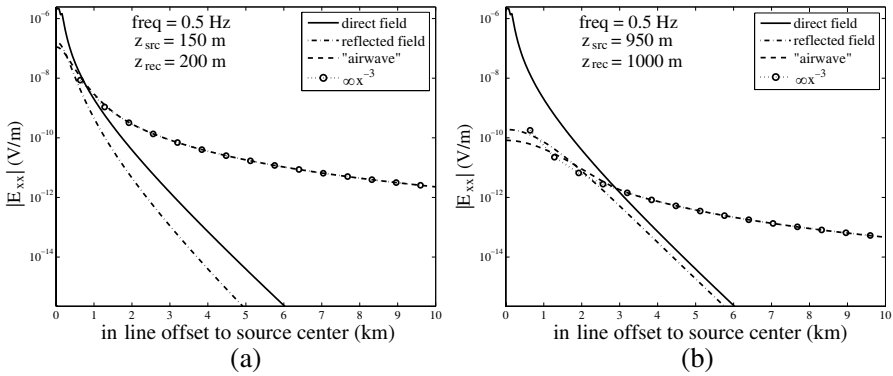

Figure 2. The amplitudes of the direct field, the specular reflection, and the contribution from the airwave as a function of horizontal offset for a vertical distance between source and receivers of 50 m, and a source at 150 m depth (a), and a source at 950 m depth (b).

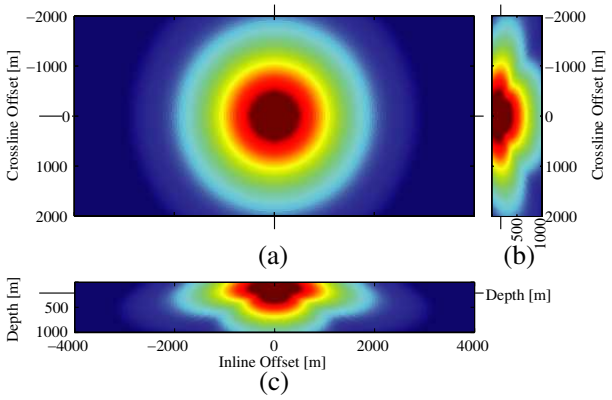

Figure 3. Total electric field in the frequency domain generated by a vertical source in a borehole at a depth of 150 m. The color scale is chosen such that all amplitudes higher than 10^{-8} V/m are saturated red and all amplitudes below 10^{-11} V/m are saturated blue. The black lines on the sides indicate the cuts of the cross sections.

contributions, the direct field from source to receiver can be separated from the specular reflection and the effect of the airwave. This is shown in Figure 2, where the x-component of the electric field at 200 m depth generated by an x-directed electric dipole source of 200 m length at 150 depth as well as the field at 1 km depth for a dipole at 950 m are shown. In the figure, the direct field is given in solid lines, the specular

reflection in dash dotted lines and the airwave effect in dashed lines. By comparing the three contributions it can be observed that the direct field is dominant in the near offset range and that the contribution from the airwave becomes dominant for offsets about 3 times the depth of the source below the surface. The airwave contribution decays only as a polynomial function of horizontal offset because a large part of the distance is traveled as a wave in the non-conducting medium. As expected from the theoretical analysis, the amplitude is proportional to x^{-3}, as indicated in Figure 2. The polynomial function is shown with circular marker on a dotted line, uses the field value at a horizontal offset of 6 km and lies completely on top of the airwave contribution from a 2 km offset onward for the shallow source receiver pair (Figure 2(a)) and from a 3.5 km offset onward for the deep source receiver pair (Figure 2(b)).

For a vertical electric dipole, only the TM-mode field is excited and therefore no airwave is generated. The amplitude of the total electric field vector in the frequency domain generated by a vertical electric dipole is shown in Figure 3 in three planes. The horizontal plane shows the amplitude at a depth of 200 m below surface, hence 50 m below the source, while the vertical planes are along the inline and crossline and contain the source. The color scale is chosen such that all amplitudes higher than 10^{-8} V/m are saturated red and all amplitudes below 10^{-11} V/m are saturated blue. It can be observed that the depth penetration of the field is much less because the ratio of horizontal and vertical conductivity is a factor five.

In the time domain, the impulse response of the direct field and the direct reflected field have a time behavior that differs from the field due to the airwave. The sum of all diffusion functions $F(\tau, t)$ in Equation (46) has a late time asymptote proportional to $t^{-2.5}$, whereas the effect of the airwave has a late time asymptote proportional to t^{-3}. This difference in late time behavior can be seen in Figure 4, where the two different contributions to the x-component of the electric field generated by an x-directed electric dipole are shown separately. We use the same conductivity values as before, but now with single source receiver pairs: a source at 150 m depth and a receiver 50 m below the source and at a horizontal offset of 2 km in Figure 4(a), and a source at 950 m depth and a receiver 50 m below the source and at a horizontal offset of 4 km in Figure 4(b). For the shallow source and receiver in Figure 4(a), the airwave effect is dominant at early times, but looses its influence already when the direct and reflected fields attain their maximum value. For late times, its contribution vanishes rapidly. For the deeper source and receiver shown in Figure 4(b), the subsurface effect of the airwave never dominates but has an appreciable

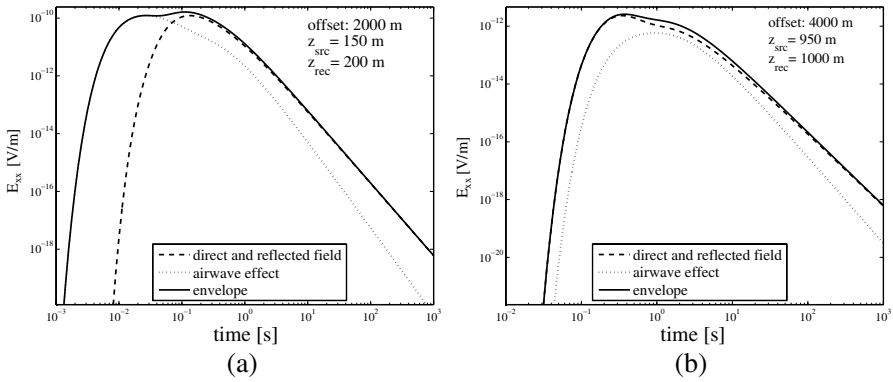

Figure 4. The impulse responses of the direct and reflected fields (dashed lines), the subsurface effect of the airwave (dotted line) and the total field (solid line) as a function of time. The vertical distance between source and receivers is 50 m. The source has a depth of 150 m and the receiver at an offset of 2 km (a), or the source has a 950 m depth and the receiver a 4 km offset (b).

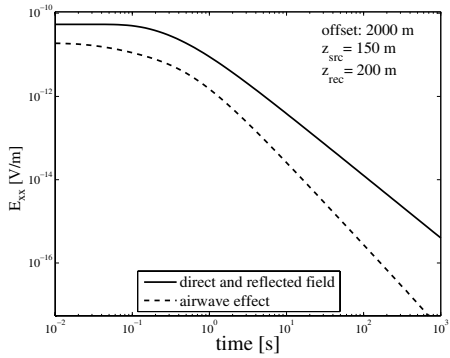

Figure 5. The step current switch off response of the direct and reflected fields (solid line), and the subsurface effect of the airwave (dashed line) as a function of time. The vertical distance between source and receivers is 50 m, and a source at 150 m depth and receiver at an offset of 2 km.

contribution in the time window that starts when the total field reaches its maximum value and continues for about 100 s after that moment. From the late time behavior of the direct and reflected fields as well as the subsurface effect of the airwave, it can be expected that the airwave effect is smallest when the step current switch off time function is used

as an excitation mechanism. This is illustrated in Figure 5 where the direct and reflected fields as well as the subsurface effect of the airwave are plotted separately for a horizontal offset of 2 km and a vertical distance between source and receiver of 50 m with the source 150 m below the surface. The airwave has a very small amplitude at the moment the source current is switched off, then remains constant for almost 1 ms, after which it starts to decrease in amplitude, first a little up to 1 s, and then proportional to t^{-2} when the late time behavior is reached. The direct and reflected fields remain strong for almost 100 ms, followed by a decay proportional to $t^{-1.5}$.

To see how the electric field vector is distributed over the half space, Figure 6 shows the impulse response electric field vector generated by an x-directed electric dipole (parallel to the inline direction) at the surface in three planes. The depth slice is taken at 200 m below the surface, and the inline and crossline depth sections contain the source. All slices are shown at 5.7 ms after the source was excited. The very strong effect of the airwave can be observed at all horizontal offsets.

Another application is the use of the analytical result in numerical modeling of the response of a heterogeneous subsurface model. In marine Controlled-Source Electro-Magnetics, a horizontal current source is usually towed at some distance above the sea bottom, while

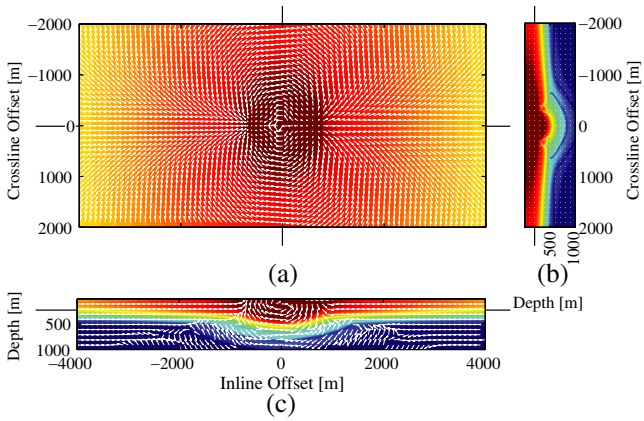

Figure 6. The electric field vector generated by an inline directed horizontal electric dipole source in a borehole at the surface. The white arrows indicate the vector directions. The color scale is chosen such that all amplitudes higher than 10^{-8} V/m are saturated red and all amplitudes below 10^{-15} V/m are saturated blue. The black lines on the sides indicate the cuts of the cross sections.

receiver antennas and coils at the sea bottom record the horizontal components of the electric and magnetic fields. The numerical simulation of these experiments, for scenario studies [24] or full blown inversion [14], requires a dense grid around the source for accurate modeling of the source singularity. In the primary-secondary formulation, the fields are split into a part that is computed analytically and a secondary part that involves the full partial differential equations driven by a source term based in the same equations applied to the primary field; see [25], for instance. This will not change the convergence rate of an iterative solution method for the discretized problem, but generally improves the accuracy of the computed target response. Also, the grid does not need to be finely sampled around the source.

As an illustration of this approach, we consider a problem with air, sea water, sediments, and a hydrocarbon reservoir. The source is located at the origin in the horizontal coordinates and at a depth of 100 m. Receivers are placed on the sea bottom at 200 m depth. The conductivity of the water is 3 S/m, the sediments have 0.5 S/m, and the reservoir 20 mS/m. The reservoir is a rectangular box between -2000 and 2000 m in x and y, and between depths of 600 and 800 m. We computed the electric fields in a range of frequencies f, on an equidistant logarithmic scale from $\log_{10} f = -3$ to $+3$ with an increment of 0.1 and frequencies in Hz, using a multigrid method [11]. The results were then interpolated by piecewise cubic Hermite interpolation to a regular frequency grid with 0.001 Hz spacing, followed by a fast Fourier transform to obtain the temporal response [12]. Although this method is more costly than the use of a Fourier transform for data on a logarithmic scale [26, 27], the result tends to be more accurate.

Figure 7 shows the inline electric field component as a function of frequency for a unit dipole current source in the x-direction. The receiver is located at $x = 400$ m, $y = 0$ m, and $z = 200$ m on the sea bottom. The full numerical solution was computed on a grid with 64^3 cells. The cell width was 100 m in the rectangular region defined by $|x| \leq 2000$ m, $|y| \leq 2000$ m, and $0 \leq z \leq 800$ m. Grid stretching was applied outside this box to place the perfectly electric conducting domain boundaries at a sufficiently large distance. We also computed the secondary solution on the same grid as well on a finer grid with 256^3 cells and spacing of 20 m in the interior part. The last one should be much more accurate and serves as a reference. From Figure 7, we can conclude that the primary-secondary solution provides a more accurate result than the full solution. Figure 8 shows the response after transformation to the time domain. For the primary-secondary

formulation, we transformed only the secondary solution and then added the primary solution in the time domain. Again, the latter provides a more accurate result than the full solution, taking the fine grid primary-secondary solution as a reference.

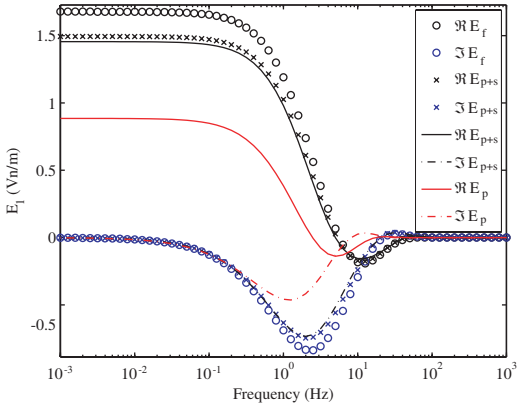

Figure 7. Frequency domain solution at a single receiver. The circles represent the full field, the crosses mark the result of the primary-secondary formulation. The primary field is drawn in red and the fine grid primary-secondary result is represented by black lines.

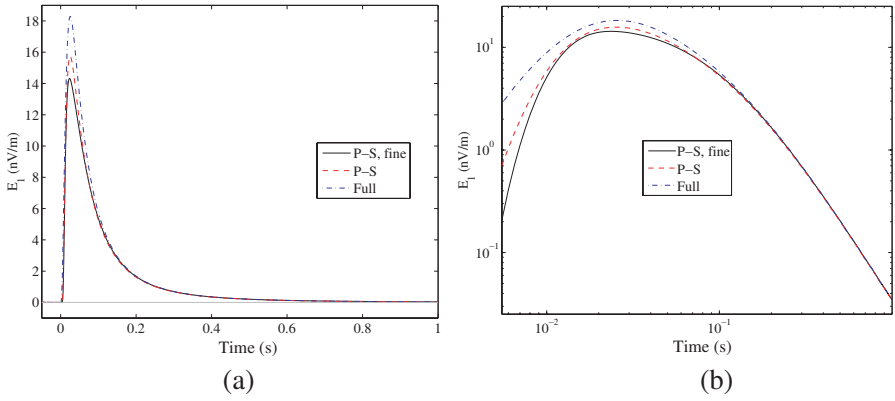

Figure 8. Time domain solution. The primary-secondary result appears to be more accurate then the full solution, when compared to the fine grid result. The panel on the right hand side has a log-log scale.

6. CONCLUSION

The diffusive electric field Green tensor was found in explicit form in space frequency and space time domains. This has advantages for integral equation modeling, because then the Green function is directly known and does not need to be computed by numerical integration techniques. Numerical results have shown that the subsurface effects of the airwave dominates the received signal when the source and receiver are close to the surface and the source operates at a single frequency. For transient electromagnetic applications, the step-current switch-off source function reduces the influence of the airwave in the whole time window of interest. It is also advantageous for the primary-secondary field implementations of finite-difference, finite-element, or finite-volume modeling schemes, because when the source function can be incorporated exactly, the grid spacings can be relaxed and due to the fact that the primary field has a very high amplitude relative to the target response, the solution for the target response is obtained with higher accuracy.

ACKNOWLEDGMENT

This work is part of the research program of the Netherlands research center for Integrated Solid Earth Science (ISES). JH receives support from the Dutch Technology Foundation STW, applied science division of NWO and the Technology Program of the Ministry of Economic Affairs.

APPENDIX A. EXPONENTIAL DIFFUSION FUNCTIONS

All terms in electromagnetic diffusive fields containing exponential and polynomial functions in space-frequency domain have explicit time-domain equivalents. These can be grouped with diffusion functions of the form

$$\hat{F}^m(s,\tau) = s^{m/2}\exp(-2\sqrt{s\tau}), \quad m \in \mathbb{Z}, \tag{A1}$$

that have time-domain equivalents given in recursive form

$$F^m(t,\tau) = \frac{\sqrt{\tau}}{t}F^{(m-1)}(t,\tau) - \frac{m}{2t}F^{(m-2)}(t,\tau), \tag{A2}$$

which can all be obtained if the ones for $m = -2$ and $m = -1$ are known. The ones that are needed for impulse and step responses are

given by

$$F^{(-2)}(t,\tau) = \operatorname{erfc}(\sqrt{\tau/t}), \tag{A3}$$

$$F^{(-1)}(t,\tau) = \sqrt{\frac{1}{\pi t}}\exp(-\tau/t)H(t), \tag{A4}$$

$$F^{(0)}(t,\tau) = \sqrt{\frac{\tau}{\pi t^3}}\exp(-\tau/t)H(t), \tag{A5}$$

$$F^{(1)}(t,\tau) = \left(\frac{\tau}{t} - \frac{1}{2}\right)\sqrt{\frac{\tau}{\pi t^3}}\exp(-\tau/t)H(t), \tag{A6}$$

$$F^{(2)}(t,\tau) = \left(\frac{\tau}{t} - \frac{3}{2}\right)\sqrt{\frac{\tau}{\pi t^5}}\exp(-\tau/t)H(t). \tag{A7}$$

The function $\operatorname{erfc}(\chi)$ is the complementary error function, defined by

$$\operatorname{erfc}(\chi) = \frac{2}{\sqrt{\pi}}\int_{u=\chi}^{\infty}\exp\left(-u^2\right)du, \tag{A8}$$

and $H(t)$ denotes the unit step function.

REFERENCES

1. Ellinsgrub, S., T. Eidesmo, S. Johansen, M. C. Sinha, L. M. MacGregor, and S. Constable, "Remote sensing of hydrocarbon layers by sea bed logging (SBL): Results from a cruise offshore Angola," *The Leading Edge*, Vol. 21, 972–982, 2002.
2. Kong, F. N., H. Westerdahl, S. Ellingsrud, T. Eidesmo, and S. Johansen, "'Seabed logging': A possible direct hydrocarbon indicator for deepsea prospects using EM energy," *Oil & Gas Journal*, Vol. 100, No. 19, 30–35, 2002.
3. Orange, A., K. Key, and S. Constable, "The feasibility of reservoir monitoring using time-lapse marine CSEM," *Geophysics*, Vol. 74, No. 2, F21–F29, 2009.
4. Zhdanov, M. S., S. K. Lee, and K. Yoshioka, "Integral equation method for 3D modeling of electromagnetic fields in complex structures with inhomogeneous background conductivity," *Geophysics*, Vol. 71, No. 6, G333–G345, 2006.
5. Van den Berg, P. M., A. Abubakar, and T. M. Habashy, "An efficient 3D integral equation method for computation of electromagnetic wavefields in a layered configuration containing inhomogeneous objects," *PIERS Proceedings*, 11–16, Cambridge, USA, July 2–6, 2008.

6. Fan, Z. H., R. S. Chen, H. Chen, and D. Z. Ding, "Weak form nonuniform fast Fourier transform method for solving volume integral equations," *Progress In Electromagnetics Research*, Vol. 89, 275–289, 2009.
7. Sun, X. Y. and Z. P. Nie, "Vector finite element analysis of multicomponent induction response in anisotropic formations," *Progress In Electromagnetics Research*, Vol. 81, 21–39, 2008.
8. Tehrani, A. M. and E. Slob, "Fast and accurate three-dimensional controlled source electromagnetic modelling," *Geophysical Prospecting*, in press, 2010, DOI: 10.1111/j.1365-2478.2010.00876.x.
9. Commer, M. and G. Newman, "A parallel finite-difference approach for 3D transient electromagnetic modeling with galvanic sources," *Geophysics*, Vol. 69, No. 5, 1192–1202, 2004.
10. Commer, M. and G. A. Newman, "An accelerated time domain finite difference simulation scheme for three-dimensional transient electromagnetic modeling using geometric multigrid concepts," *Radio Science*, Vol. 41, No. 3, RS3007, 2006.
11. Mulder, W. A., "A multigrid solver for 3D electromagnetic diffusion," *Geophysical Prospecting*, Vol. 54, No. 5, 633–649, 2006.
12. Mulder, W. A., M. Wirianto, and E. C. Slob, "Time-domain modeling of electromagnetic diffusion with a frequency-domain code," *Geophysics*, Vol. 73, No. 1, F1–F8, 2008.
13. Commer, M. and G. A. Newman, "New advances in three-dimensional controlled-source electromagnetic inversion," *Geophysical Journal International*, Vol. 172, No. 2, 513–535, 2008.
14. Plessix, R.-É. and W. A. Mulder, "Resistivity imaging with controlled-source electromagnetic data: Depth and data weighting," *Inverse Problems*, Vol. 24, No. 3, 034012, 2008.
15. Abubakar, A., T. M. Habashy, M. Li, and J. Liu, "Inversion algorithms for large-scale geophysical electromagnetic measurements," *Inverse Problems*, Vol. 25, No. 12, 123012, 2009.
16. Newman, G. A., M. Commer, and J. J. Carazzone, "Imaging CSEM data in the presence of electrical anisotropy," *Geophysics*, Vol. 75, No. 2, F51–F61, 2010.
17. Raiche, A. P. and J. H. Coggon, "Analytic Greens tensors for integral-equation modeling," *Geophysical Journal of the Royal Astronomical Society*, Vol. 42, No. 3, 1035–1038, 1975.
18. Kong, J. A., "Electromagnetic fields due to dipole antennas over stratified anisotropic media," *Geophysics*, Vol. 37, No. 6, 985–996, 1972.

19. Gradshteyn, I. S. and I. M. Ryzhik, *Tables of Integrals, Series, and Products*, 5th Edition, Academic Press, New York, 1996.
20. Abramowitz, M. and I. A. Stegun, *Handbook of Mathematical Functions*, 10th edition, Applied Mathematics Series 55, National Bureau of Standards, Washington, USA, 1972.
21. Oberhettinger, F. and L. Badii, *Tables of Laplace Transforms*, 1st edition, Springer-Verlag, Berlin, 1973.
22. Gaver, D. P., "Observing stochastic processes and approximate transform inversion," *Operations Research*, Vol. 14, No. 3, 444–459, 1966.
23. Stehfest, H., "Numerical inversion of Laplace transforms," *Communications of the ACM*, Vol. 13, No. 1, 47–49, 1970.
24. Plessix, R.-É., M. Darnet, and W. A. Mulder, "An approach for 3D multisource, multifrequency CSEM modeling," *Geophysics*, Vol. 72, No. 5, SM177–SM184, 2007.
25. Wirianto, M., W. A. Mulder, and E. C. Slob, "A feasibility study of land CSEM reservoir monitoring in a complex 3-D model," *Geophysical Journal International*, Vol. 181, No. 2, 741–755, 2010.
26. Talman, J. D., "Numerical Fourier and Bessel transforms in logarithmic variables," *Journal of Computational Physics*, Vol. 29, No. 1, 35–48, 1978.
27. Haines, G. V. and A. G. Jones, "Logarithmic Fourier transformation," *Geophysical Journal of the Royal Astronomical Society*, Vol. 92, 171–178, 1988.